Interpenetrating network-based hybrid solid and gel electrolytes for high voltage lithium metal batteries

Yongwei Zheng,[†] *Xiaowei Li,*[†] *Will Fullerton,*[†] *Qian Qian,*[†] *Mingwei Shang,*[‡] *Junjie Niu*[‡] *and Christopher Y. Li**[†]

[†] Department of Materials Science and Engineering, Drexel University, Philadelphia, PA 19104, USA

[‡] Department of Materials Science and Engineering, University of Wisconsin-Milwaukee, Milwaukee, WI 53211, USA

KEYWORDS: solid polymer electrolytes, network solid polymer electrolytes, lithium metal batteries, lithium dendrites, high voltage lithium batteries

Abstract: Solid-state lithium metal battery (SSLMB) is a desired future energy supply choice because of its improved safety and higher energy density compared with traditional liquid electrolyte-based lithium ion batteries. Poly(ethylene oxide) (PEO)-based network solid polymer electrolytes (SPEs) have recently attracted increasing attention in the research field due to their low cost, chemical versatility, excellent lithium dendrite resistance, and good device cyclability. However, the low anodic stability renders this system incompatible with high voltage cathodes, such as lithium nickel manganese cobalt oxides. In this work, we tackled this problem by

introducing an interpenetrating network (IPN) consist of a primary PEO-contained network SPE and a linear poly(acrylonitrile) (PAN) secondary network. The chemical and architectural nature of these IPN-SPEs allowed us to significantly increase the oxidative stability of the SPEs from 4.1 V to over 5.1 V by incorporating only 2 wt.% of PAN. The IPN network can be used as both SPE as well as the host to form gel electrolytes. In SSLMBs based on the IPN-SPEs, lithium metal anodes, and $LiNi_{0.6}Mn_{0.2}Co_{0.2}O_2$ cathodes, a capacity of over 150 mAh g^{-1} was achieved at 90 °C with excellent cyclability. By infiltrating diglyme-based liquid electrolytes into IPN-SPEs, a gel electrolyte was formed with excellent electrochemical properties and high conductivity at room temperature. LMBs using such electrolytes delivered a capacity of over 170 mAh g^{-1} with excellent Coulombic efficiency and cycling stability. Our study demonstrated that the IPN-based SPEs are promising to address the challenges of high voltage secondary batteries.

Introduction

Novel materials for lithium batteries (LBs) with improved working voltage, energy, and power delivery have been developed and successfully commercialized during the past three decades.[1-2] Improving battery safety is another essential target for the LB development. The origin of the potential fire hazard associated with LBs arises from the flammable organic carbonate-based liquid electrolytes and lithium dendrite-induced cell short-circuit.[3-5] The latter could be more detrimental to the device when Li metal is used as the anodes. Besides the safety issue, Li dendrite growth in LBs could also break the solid electrolyte interface (SEI), accelerate side reactions, and

increase polarization resistance, thus resulting in a reduced Coulombic efficiency (CE) and decayed capacity.[6-10] Recently, researchers have demonstrated that substituting liquid electrolytes with solid polymer electrolytes (SPEs) is a viable way to fabricate solid-state lithium metal batteries (SSLMBs) where Li dendrite formation can be effectively retarded.[11-12] Among various choices of SPEs, poly(ethylene oxide) (PEO)-based network electrolytes stand out due to the collective property control among ionic conductivity, mechanical strength, high chain flexibility, chemical tunability, and good manufacturing control.[13-19] Unfortunately, the low anodic stability and oxidative breakdown of PEO limit its application to below 4.0 V, which restricts the selection of cathode materials to lithium iron phosphate (LFP) in most reported work.[12-13, 15] However, the average 3.3-3.4 V discharge voltage delivered by LFP cannot satisfy high energy and power density needs for many applications. Therefore, the field calls for new SPEs that are compatible with high voltage cathodes.

The principal strategies of increasing SPE's anodic stability include modifying SPE chemical structure or introducing small molecular additives.[20-22] Studies have shown that poly(sulfone) (PSU)-based and PAN-based polymers can be stable to over 5 V.[23-27] However, the rigidity of the chains and high glass transition temperature (PSU ~ 185 ºC, PAN ~ 95 ºC) hinder ionic transport and undermine an otherwise conformal coating layer between SPE and the electrode.[28-29] Recently reported comb-chain crosslinker based network SPEs showed high oxidative stability.[30] On the other hand, introducing salt additives has already been an effective way to tune properties in the liquid electrolyte field. For example, the addition of lithium nitrate ($LiNO_3$) in dioxolane/dimethoxyethane (DOL/DME) based electrolytes can facilitate the formation of a stable SEI on the Li metal anode and improve the cycling stability of Li-S batteries.[31-32] Recently, Choudhury *et al.* reported that the addition of lithium bis(oxalate)borate

(LiBOB) in diglyme can increase the anodic limit from 4.2 V to 4.6 V. By combining with a $LiNi_{0.6}Mn_{0.2}Co_{0.2}O_2$ cathode, the electrolyte can deliver a capacity of over 150 mAh g^{-1} after 200 cycles at 0.2 C.[33] Zhao *et al.* synthesized composite SPEs using triple salts including bis(trifluoromethanesulfonyl)imide (LiTFSI), LiBOB and $LiNO_3$, which could pair with $LiNi_{0.33}Mn_{0.33}Co_{0.33}O_2$ cathodes and delivered a capacity over 100 mAh g^{-1} for 60 cycles at 0.2 C.[34] In general, the working mechanism of salt additives is through tuning the interfacial chemistry on the electrode surface, forming a stable protective layer and preventing further decomposition of the electrolyte.[35]

In this work, we report a series of polymer interpenetration network SPEs (IPN-SPEs) with a high anodic stability voltage. As the name suggests, IPNs incorporate two or more independent networks into one materials system. The independent network chemistry can then be used to tailor the network's mechanical and electrochemical properties. In our previous studies, we reported that a polyhedral oligomeric silsesquioxane (POSS) nanoparticle-based network SPE shows superior structural robustness and Li dendrite resistance.[15] The PEO chain in the hybrid network is also compatible with conventional polar polymers to create IPNs. For example, Li^+-PEO interaction can be decoupled by introducing a poly (propylene carbonate) (PPC) secondary network, and the resultant SPE shows a tripled cation transference number.[36] In this work, we employ the POSS-based hybrid SPE as the primary network and introduce linear poly(acrylonitrile) (PAN) as the secondary network (note that it's a semi-IPN structure since PAN is not chemically crosslinked, and we use IPN herein for simplicity). PAN is chosen because it is more resilient to oxidation at high voltage due to its relatively low HOMO levels (-8.85 eV vs -7.17 eV for PEO).[37-39] Furthermore, the polar cyano group facilitates a homogeneous blend with PEO in a wide compositional range. The prepared IPN-SPE is stable at over 5 V and compatible with

$LiNi_{0.6}Mn_{0.2}Co_{0.2}O_2$ cathodes in SSLMBs. PAN can also tune the SPE|Li metal interface and improve CE (Scheme 1). In order to further enhance the ion transport and lower the battery operation temperature, high voltage gel polymer electrolyte was fabricated by soaking the IPN-SPE in diglyme-$LiNO_3$-LiBOB-based liquid electrolytes, and improved cycling performance was realized in $LiNi_{0.6}Mn_{0.2}Co_{0.2}O_2$ SSLMBs. In addition, we have systematically studied the effect of PAN, $LiNO_3$, and LiBOB on the formation of SEI.

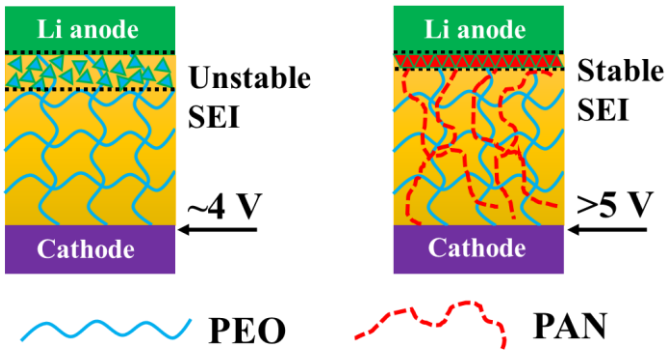

Scheme 1. Scheme of high anodic voltage and stable SEI with addition of PAN into PEO network.

Results and discussion

The IPN-SPEs were prepared using a facile one-pot synthesis method. Amine-terminated bifunctional poly (ethylene glycol) (H_2N-PEG-NH_2) (molar mass ~ 2 kg mol^{-1}) was crosslinked by epoxy-functionalized POSS in the presence of linear PAN (molar mass 150 kg mol^{-1}) and LiTFSI. The molar ratios of PEG / POSS and EO / LiTFSI were fixed at 4:1 and 10:1, respectively, because our previous study revealed that this network structure and salt concentration could deliver the best balance between ionic conductivity and mechanical properties.[15, 36] The weight concentration of PAN in the total network was tuned from 2 wt.% to 5 wt.% and 10 wt.%. In the following discussion, the samples are abbreviated as IPN-*w*PAN where *w* is the weight percent of

PAN. The chemical structure of the reagents, synthesis route, a digital photo, and a scanning electron microscopy (SEM) image of the as-prepared IPN SPEs are shown in Figure 1(a). Detailed preparation process and conditions are described in the Experimental section. Small angle X-ray scattering (SAXS) results (Figure S1) show no scattering peak and obvious upturn in the experimental length scale, confirming the absence of phase separation in the SPEs, which may be facilitated by the lithium salt/polymer interaction.[40-41] **Table 1** summarizes the physical properties of the prepared IPN-SPEs.

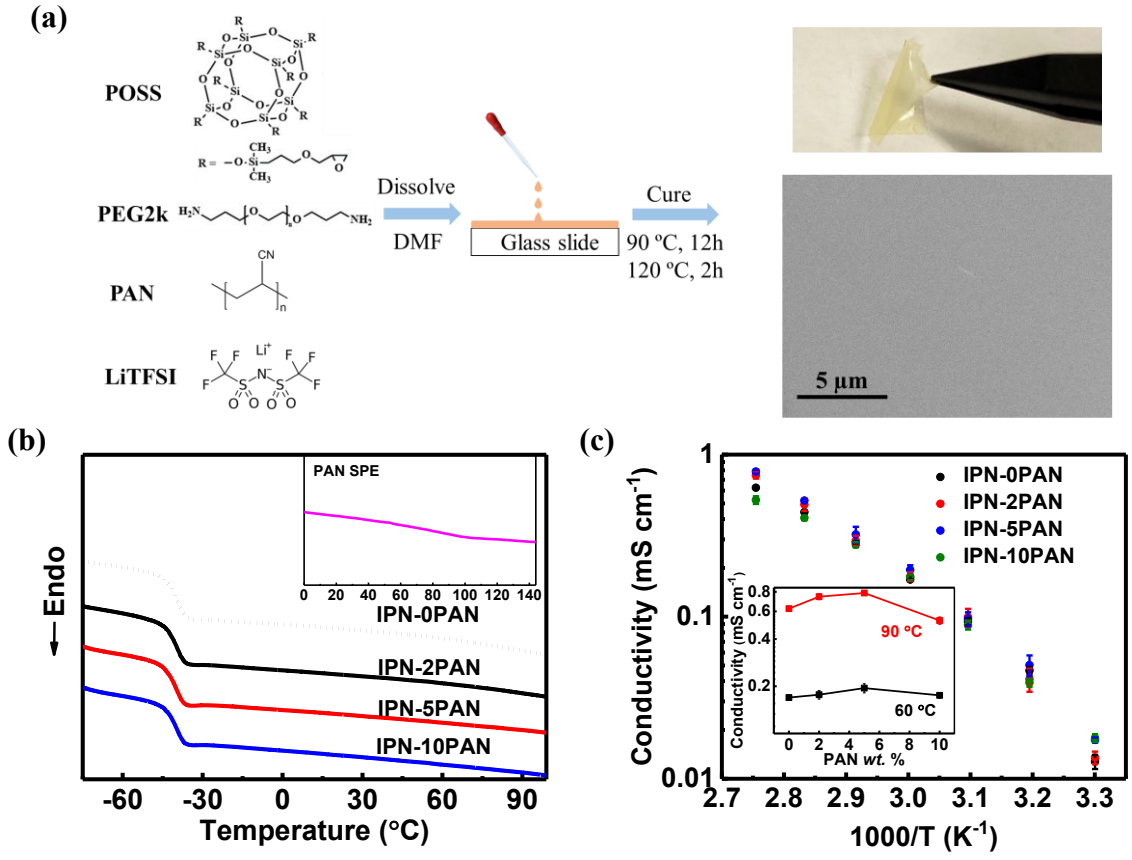

Figure 1. (a) Chemical structure, composition, synthesis route, and a digital photo of PAN-based IPN SPEs. (b) DSC thermograms of the SPEs. The inset is the DSC thermogram of the control PAN SPE in which the molar ratio between CN and LiTFSI is 10. (c) Ionic conductivity vs. temperature plot. The inset is the conductivity change with the PAN content at 60 ºC and 90 ºC.

Table 1. Physical properties of prepared SPEs.

SPE	PEG [*wt. %*][a]	PAN [*wt. %*] [b]	T_g [*ºC*] [c]	σ [$S\ cm^{-1}$] at 60 ºC [d]	σ [$S\ cm^{-1}$] at 90 ºC [d]	Oxidative voltage (V)[e]
IPN-0PAN	53.5	0	-39.2	1.69×10^{-4}	6.25×10^{-4}	4.1
IPN-2PAN	52.7	1.3	-39.3	1.77×10^{-4}	7.45×10^{-4}	5.1
IPN-5PAN	51.6	3.4	-40.2	1.95×10^{-4}	7.86×10^{-4}	5.1
IPN-10PAN	49.7	6.9	-39.6	1.75×10^{-4}	5.25×10^{-4}	5.1

a: weight percentage of PEG in total SPE (salt included)
b: weight percentage of PAN in total SPE (salt included)
c: measured by DSC heating at 10 ºC/min
d: measure by EIS
e: measured by CV

Low glass transition temperature (T_g) is typically preferred to achieve high conductivity in polymers because ion migration is facilitated through polymer chain reptation.[11, 42] Figure 1(b) shows differential scanning calorimeter (DSC) heating thermograms of the SPEs. In addition to IPN SPEs, a PAN SPE comprised of linear PAN and LiTFSI with a molar ratio of 10:1 between the CN group and LiTFSI was also tested. DSC of pure PAN is shown in Figure S2. T_g of pure PAN and PAN SPE are 101.2 ºC and 80.7 ºC, respectively. T_g of the control PAN-free network SPE, IPN-0PAN, is -39.2 ºC. With the addition of PAN, polymer T_g slightly changed to -39.3 ºC, -40.2 ºC and -39.6 ºC for IPN-2PAN, IPN-5PAN, and IPN-10PAN, respectively. Although the PAN SPE has a relatively high T_g of 80.7 ºC compared to the control IPN-0PAN (-39.2 ºC), the addition of PAN to the hybrid network only slightly affects T_g, even at 10 wt.% of PAN, indicating that PEO segments in the network dominate the glass transition behavior. The slightly decreased T_g after adding higher T_g PAN is likely due to the reduced Li+ crosslinking effect on PEO. The formation of a uniform IPN can also be confirmed because only one T_g is seen in the DSC

thermograms, consistent with the SAXS results and our previous report.[36] No crystallization/melting peaks are observed from the DSC thermograms.

The pure PAN SPE has a relatively low ionic conductivity because of its relatively rigid chain. For example, PAN doped with $LiClO_4$ can only deliver a conductivity of ~10^{-7} S cm^{-1} at room temperature.[29] Figure 1(c) shows the effect of PAN addition on the ionic conductivity of IPN SPEs. When the PAN content increases from 0 wt.% to 2 wt.% and 5 wt.%, the conductivity increases from 1.69×10^{-4} S cm^{-1} to 1.77×10^{-4} S cm^{-1} and 1.95×10^{-4} S cm^{-1} at 60 ºC, and from 6.25×10^{-4} S cm^{-1} to 7.45×10^{-4} S cm^{-1} and 7.86×10^{-4} S cm^{-1} at 90 ºC. When the PAN concentration further increases to 10 wt.%, the conductivity decreases to 1.75×10^{-4} S cm^{-1} and 5.25×10^{-4} S cm^{-1} at 60 ºC and 90 ºC, respectively. The above results indicate that the IPN SPEs deliver higher conductivity than both pure PAN and PAN-free network SPEs. To better understand the ion transport mechanism, Vogel-Tamman-Fulcher (VTF) equation was used to fit the conductivity-temperature behavior (Figure S3 and Table S1). E_a does not vary significantly as it is related to T_g which only slightly changes over the PAN concentration ranges. However, IPN-2PAN and IPN-5PAN show significantly higher A value, indicating that the determining factor of the increased conductivity in these two samples is the effective charge carrier population, which is related to A. Since both the ether groups of PEG and the cyano groups of PAN can interact with lithium cations, PAN in the network effectively pulls lithium ions away from the ether groups and liberate lithium ions. This competing effect therefore leads to a higher population of dissociated ions and facilitates ion transport in the polymer matrix. As the PAN concent further increases to 10 wt.%, the PAN chains could impose steric hindrance for lithium ion hopping in PEO, therefore reduces ion conductivity.

Cyclic voltammetry (CV) was used to measure the anodic stability (Figure 2a and Figure S4) of the SPEs. The control network IPN-0PAN was stable up to 4.1 V, which is consistent with our previous report.[15] For IPN-2PAN, IPN-5PAN, and IPN-10PAN, no oxidative current was observed below 5.1 V. With the increase of cycling number, the oxidative current intensity decays which indicates that PAN facilitates the formation of a protective layer on the cathode surface and prevents further oxidation. The stable potentials of IPN-2PAN, IPN-5PAN, and IPN-10PAN are all 5.1 V, which reveals that as low as 2% of PAN is sufficient to significantly increase the anodic stability. Since IPN-5PAN has a slightly lower T_g and higher ionic conductivity, it will be used for further electrochemistry tests in the following study.

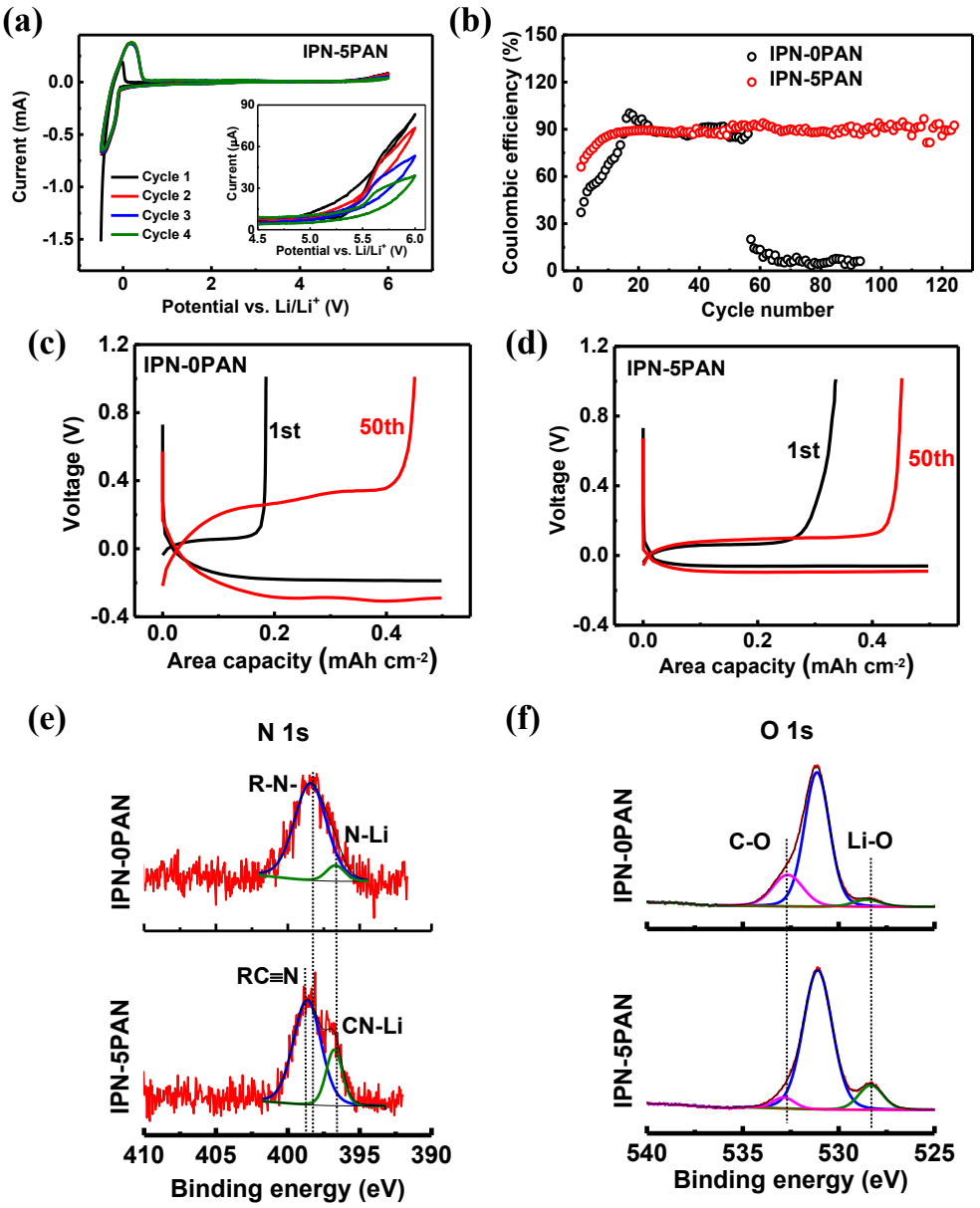

Figure 2. (a) Cyclic voltammetry of a cell with configuration Li|IPN-5PAN|stainless steel for 4 cycles between -0.5 V and 6 V. The scan rate is 0.5 mV s^{-1}. (b) Coulombic efficiency measurement of Li|SPE|Cu asymmetrical cell using IPN-0PAN and IPN-5PAN as electrolyte. The current density and capacity are 0.5 mA cm^{-2} and 0.5 mAh cm^{-2}. The voltage profiles of plating and stripping process from 1st and 50th cycle for electrolyte using IPN-0PAN (c) and IPN-5PAN (d). XPS spectra of (e) N 1s and (f) O 1s of cycled lithium metal surface from Li|SPE|Cu cells using IPN-0PAN and IPN-5PAN. The surface was etched by a 2 kV Ar ion gun for 1 min.

The effect of PAN on the lithium anode interface was evaluated using a lithium plating/stripping test in an asymmetrical Li|SPE|Cu cell at 90 ºC. With a lithium plating capacity of 0.5 mAh cm^{-2} at a current density of 0.5 mA cm^{-2}, CE was estimated based on the charge transferred in a stripping process over that in the previous plating process. Figure 2(b) shows the CE of the cells using IPN-0PAN and IPN-5PAN. For IPN-5PAN, CE became stable after 10 cycles and maintained stable for over 100 cycles. The average CE after 10 cycles was 89.6% with a standard deviation of 2.3%. On the other hand, it took more than 20 cycles for the CE of IPN-0PAN cells to stabilize and the CE significantly dropped after 55 cycles. Figures 2c and d show the voltage profile of the 1^{st} and 50^{th} cycles for each cell. Comparing the 1^{st} and 50^{th} cycle, the hysteresis remained nearly constant for the cell using IPN-5PAN (124 mV to 193 mV) while it significantly increased (205 mV to 573 mV) for the IPN-0PAN cell. These results demonstrate that the addition of PAN facilitates the formation of a stable SEI and reduces the interface resistance. To further understand the SEI's chemical component, X-ray photoelectron spectroscopy (XPS) was conducted on the lithium metal surface after 50 cycles of the plating/stripping test. Figure 2(e) and (f) showed the XPS spectra of O 1s and N 1s and Figure S5 show the XPS spectra of C 1s, F 1s, and S 2p. The lithium metal surface was sputtered by 2 kV Ar ion for 1 min to remove the residue SPE and assure the measured signal is from the SEI layer. The binding energy was calibrated by C 1s (284.6 eV). Table S2 summarizes the binding energy of each chemical compound that appears in this work. For N 1s signal from the IPN-0PAN cell, two peaks can be used to fit the curve. The main peak is N binding with C and can be attributed to the amine group (RNH- or -(R)N-), decomposed from the PEO chains. The peak is broad because it's a mixture of secondary and tertiary amine.[43] For N 1s signal from cell using IPN-5PAN, two peaks are also seen. Compared with IPN-0PAN, the main peak became narrower and shifted to a higher

binding energy direction, which can be attributed to the cyano group (-C≡N).[43] The other peak with a lower binding energy is metallic N (Li_3N). The peak of metallic N is much stronger from the cell using IPN-5PAN. That is because first, the cyano group can be considered as a Lewis base and interact with Li^+. Second, Li_3N is the reduced product from LiTFSI.[31] The lone electron pair of the cyano group could facilitate this process. From O 1s signal, more metal-bonded O, associated with the reduction process of LiTFSI, exists in SEI of the cell using IPN-5PAN while stronger signal from ether group (C-O-C) is observed in SEI of the cell using IPN-0PAN. C-O-C can be decomposed to C-O-H. The accelerated reduction and decomposition induced by cyano group could produce more metal-bonded O / C-O-H and less C-O-C in the SEI. In brief, XPS data reveals that when PAN is added, the cyano groups facilitate the electrolyte reduction and the formation of the SEI rich in metallic N and metallic O. It also explains why in Figure 2(b), it takes less cycles to stabilize the CE. The reconstructed SEI structure is consistent with our previously reported work that the inner layer of SEI is rich in inorganic species covering Li metal anode and the outer layer of SEI is rich in organic species.[36] A recent study using in situ liquid secondary ion mass spectrometry also observed a similar hierarchical SEI structure in the lithium bis(fluorosulfonyl)imide (LiFSI) / DME system. The dense organic inner layer is mechanically more stable and ionically more conductive, which can more effectively stabilize the lithium metal anode.[44] The cycled Li metal surfaces were observed under SEM (Figure S6). Though rough as well, slightly less nucleation sites were observed for the cell using IPN-5PAN after 120 cycles. The galvanostatic symmetrical Li|SPE|Li cell cycling also demonstrated good compatibility between Li metal anode and IPN-5PAN SPE (Figure S7).

To evaluate the performance of full batteries, we assembled SSLMBs using $LiNi_{0.6}Mn_{0.2}Co_{0.2}O_2$ cathodes,[58-60] lithium metal anodes, and IPN-5PAN as both the electrolytes

and separator. $LiNi_{0.6}Mn_{0.2}Co_{0.2}O_2$ was synthesized using a coprecipitation and calcination method.[45] Figure S8 shows the SEM images of the $LiNi_{0.6}Mn_{0.2}Co_{0.2}O_2$ particles which are uniform in size. The phase structure was confirmed by X-ray diffraction (XRD) (Figure S9). The composite cathode consists of $LiNi_{0.6}Mn_{0.2}Co_{0.2}O_2$ particles, poly (vinylidene difluoride) (PVDF), and carbon black in a weight ratio of 8:1:1. The SSLMB was galvanostatically cycled between 2.5-4.2 V at a current rate of 20 mA g^{-1} (0.1 C, 1 C = 200 mAh g^{-1}) at 90 ºC. An initial discharge capacity of 151 mAh g^{-1} was obtained, and after 50 cycles, the discharge capacity decayed to 122 mAh g^{-1} and retained at 80.3%. The average CE during the 50 cycles is 98.4%. Literature reports on SSLMBs using NMC-family ($LiNi_xMn_yCo_zO_2$, x+y+z=1) as cathode are rare.[34, 46-47] Zhao *et al.* synthesized PEO composite SPE with halloysite nanoclay and three salt additives and reported a specific capacity of 100 mAh g^{-1} after 60 cycles using $LiNi_{0.33}Mn_{0.33}Co_{0.33}O_2$ as cathode material.[34] The reported CE is about 99% which is slightly higher than ours. Previous study also showed unstable CE at elevated temperature for the cathode from NMC-family.[48] Compared with $LiNi_{0.33}Mn_{0.33}Co_{0.33}O_2$, $LiNi_{0.6}Mn_{0.2}Co_{0.2}O_2$ has a higher Ni concentration and can deliver a higher capacity. As a trade-off, it also increases the structural instability and thus deteriorate the cycle stability. Overall, the present SSLMBs show a superior capacity retention rate and we anticipate that improved conductivity and more efficient ion transport of SPE could further improve CE..[49]

In addition to capacity decay, nominal voltage is another critical parameter to evaluate batteries, which is related to the energy and power of the battery. Here we use the evolution of midpoint voltage in the discharge step to demonstrate nominal voltage decay. The midpoint voltage is defined as the voltage when the capacity reaches half of the full capacity. Figure 3c shows the midpoint voltage with the cycle number. The initial midpoint voltage is 3.71 V and after 50 cycles, the voltage decreases to 3.63 V, retaining 97.9% of the original value. It has been

reported that an initial midpoint voltage of around 3.6 V decayed to around 3.5 V after 50 cycles for $LiNi_{0.33}Mn_{0.33}Co_{0.33}O_2$ using PEO composite SPE.[34] Our SSLMBs exhibit a stable midpoint voltage above 3.6 V during the entire cycle life. A previous study showed that for LIBs using $LiNi_{0.6}Mn_{0.2}Co_{0.2}O_2$ as the cathode, nominal voltage decay is caused by the growth of interface on both anodes and cathodes as well as the increased charge-transfer resistance.[50] Figure S10 shows the Nyquist plot of the battery before cycle (25.1 ohms), after 10 cycles (219.4 ohms), and 50 cycles (289 ohms). There is only a slight increase of resistance from 10 cycles to 50 cycles. Herein, the stabilized interface in our SSLMBs accounts for the low midpoint voltage decay. On the other hand, the mechanism of capacity decay is much more complicated and controversial. One reason is the loss of lithium inventory which is associated with SEI growth and lithium plating. Besides , the Li^+ and Ni^{2+} mixing will cause the capacity and voltage midpoint decay which is a common fading mechanism for Ni-rich cathodes.[51] Another reason is that PVDF is used as a binder, which is a poor ionic conductor.[52] At increased cycle number, Li^+ insertion into cathode could be less efficient due to the sluggish Li+ diffusion through PVDF, which indirectly cause the loss of lithium inventory. A recent study also proposed that the degradation at a high state of charging is induced by the mismatch in surface reconstruction for Ni-rich cathodes.[53] In general, our designed IPN-SPE is not targeted for addressing the above issue, and as shown in Figure 3d, capacity decay should be improved in the future study.

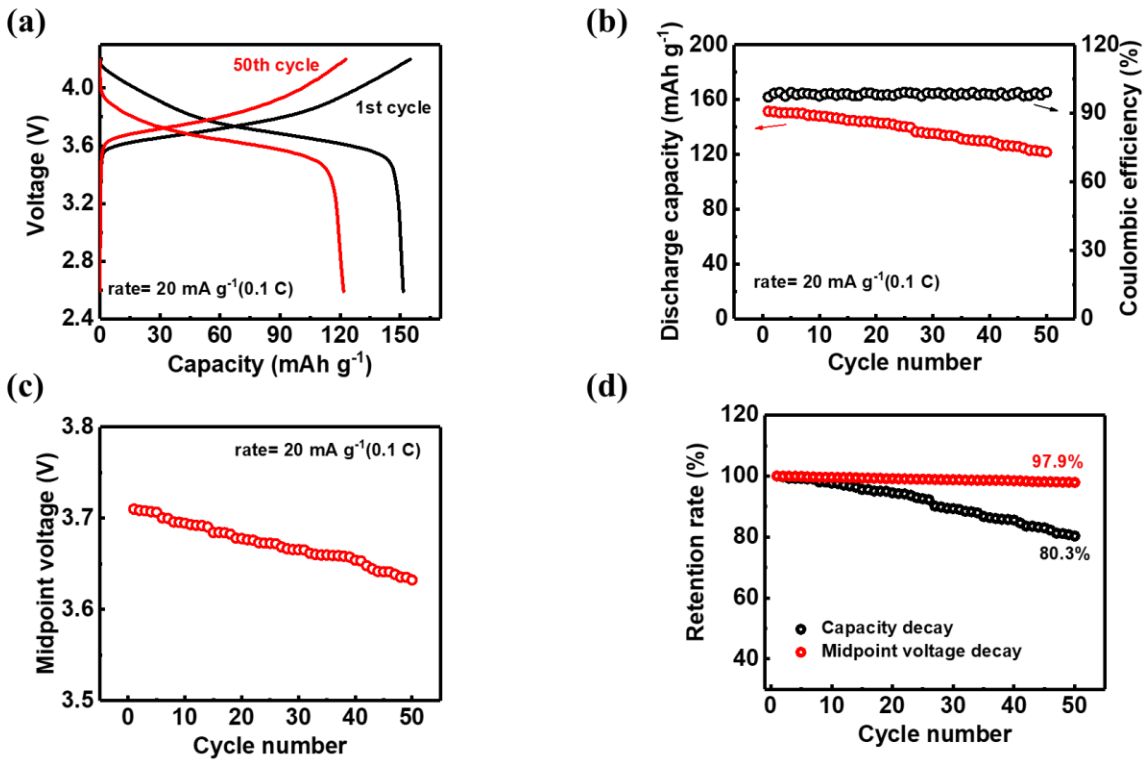

Figure 3. Performance of SSLMBs $LiNi_{0.6}Mn_{0.2}Co_{0.2}O_2$ | IPN-5PAN |Li working at 90 ºC. The current rate is 20 mA g^{-1} or 0.1 C. (a) Charge/discharge profiles from the 1st and 50th cycles. (b) Cycling stability of discharge capacity and CE. (c) Cycling stability of discharge midpoint voltage. (d) Capacity and voltage retention rates.

Room temperature high voltage LMB

One issue of the above-discussed SSLMB is that it can only work at high temperatures (*e.g.* 90 °C). The relatively low ionic conductivity of SPE prevents it from room temperature applications. To this end, we further built on the IPN-SPE platform and fabricated IPN-based high voltage gel polymer electrolytes (GPEs) by soaking IPN-5PAN in diglyme-$LiNO_3$-LiBOB liquid electrolytes, and the resulted SPE is abbreviated as IPN-5PAN-G. The molar ratio between $LiNO_3$ and EO is 0.1, and the concentration of LiBOB is 0.4 M. CE of lithium plating/stripping was first measured to evaluate the stability between IPN-5PAN-G and the lithium metal anode. A Celgard

membrane soaked in LP40 (EC/DEC 1:1 vol/vol + 1M $LiPF_6$) was selected as the control electrolyte. The plating capacity was fixed at 0.5 mAh cm^{-2}, a current density of 0.5 mA cm^{-2} was used, and all the measurements were conducted at 25 ºC. Figure 4a shows the CE with cycling number for the cell using IPN-5PAN-G and the control electrolyte. The CE of the IPN-5PAN-G cell quickly reached over 95% after 5 cycles and the cell was stably cycled for 250 cycles with an average CE of 98.7%. By comparison, the cell using the control electrolyte could only deliver the highest CE of 90% and remain stable for 25 cycles before the CE dropped to 50%. This result is consistent with the previous report that using LP 40 with 2 wt.% vinylene (VC) carbonate additive, where CE quickly dropped after 50 cycles at 0.25 mAh cm^{-2} and 40 cycles at 0.5 mAh cm^{-2}.[54] Figures 4b and 4c show the capacity-voltage profile in 2^{nd}, 10^{th} and 50^{th} cycles of the cell using the control electrolyte and IPN-5PAN-G, respectively. The hysteresis of the cell using the control electrolyte increased from 51 mV to 59 mV and 330 mV when the cycle number increases from 2 to 10 and 50. During the same cycle range, the hysteresis of the IPN-5PAN-G cell decreased from 220 mV to 165 mV and 85 mV. Therefore, compared with the control electrolyte, IPN-5PAN-G can effectively stabilize the interface with lithium metal anode, prevent SEI breaking, and mitigate the ion transport resistance increase at the interface. The surface morphology of cycled Li metal anode was also characterized by SEM (Figure S11). The control electrolyte results in a tubular protruding morphology after 50 cycles. On the other hand, after 250 cycles, the Li metal anode surface displays a much denser morphology with IPN-5PAN-G. Though lithium particles are detected, the shape is more granule-like with a lower aspect ratio.

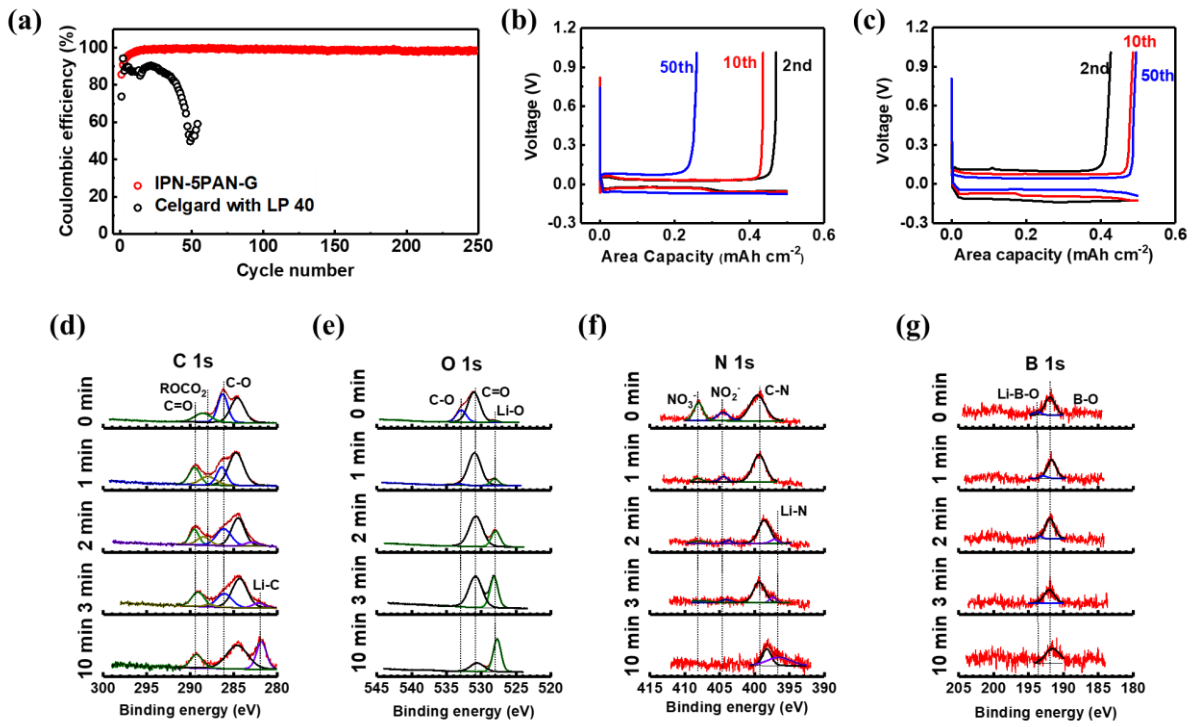

Figure 4. (a) Coulombic efficiency measurement of Li|Cu asymmetrical cell using IPN-5PAN-G and control electrolyte. The current density and capacity are 0.5 mA cm^{-2} and 0.5 mAh cm^{-2}. The voltage profiles of plating and stripping process from 2^{nd}, 10^{th} and 50^{th} cycle for electrolyte using control electrolyte (b) and IPN-5PAN-G (c). XPS spectra of (d) C 1s, (e) O 1s, (f) N 1s, and (g) B 1s of cycled lithium metal surface from Li|Cu cells using IPN-5PAN-G. The surface was etched by a 2 kV Ar ion gun for 0 min, 1 min, 2 min, 3 min, and 10 min.

The stable cycling of the lithium metal anode is mainly due to the stable SEI formed. To evaluate the formation and components of the SEI, an XPS depth profile was recorded on the lithium metal surface after 50 cycles. Ar ion was used to etch the surface for different times, from 1 min to 10 min. Figure 4d-g shows the XPS spectra of C 1s, O 1s, N 1s, and B 1s acquired after 0 min, 1 min, 2 min, 3 min, and 10 min sputtering. All peaks were calibrated by C-C signal (284.6 eV). From C 1s signal, the peak of carbonyl group (C=O) exists in SEI from 0 min to 10 min sputtering while the peak of ether group (C-O) gradually decreases and disappears with increased sputtering time. This is consistent with the O 1s signal. C=O group is decomposed from BOB^- and

C-O group is mainly from PEO. This demonstrated that the organic reduction product (RCH_2OLi) only exists on the very top of the SEI layer. From O 1s and N 1s signal, the generation of Li_2O and the evolution of N, from $LiNO_3$ to $LiNO_2$ and Li_3N are clearly shown. When the sputtering time is over 2 min, especially at 10 min, the Li_2O peak becomes dominant and the intensity of Li_3N peak increased (by 1.6 time between 2 min and 10 min). From the B 1s signal, the intensity of the B signal remained nearly unchanged with the sputtering time. Compared with lithium metal bonded B, non-metallic BOB^- is the main product.[33] Therefore, the structure of the SEI on the lithium metal anode can be constructed. The inner layer of SEI (near lithium metal anode) mainly consists of inorganic Li_3N and Li_2O which forms a strong layer and covers the lithium metal anode. The outer layer of SEI mainly consists of organic components decomposed from the polymer matrix. The reduction products from LiBOB exist in the entire SEI layer. In comparison, many previous studies have confirmed that the main decomposition products from LP 40 on lithium metal anode are loosely packed alkyl carbonate and Li_2CO_3. $(CH_2OCOOLi)_2$ is the main reduced component from EC while $LiPF_6$ can be reduced to inorganic components following the equation (1) and (2).

$$LiPF_6 \longrightarrow LiF\ (s) + PF_5\ (g) \qquad (1)$$

$$LiPF_6 + H_2O \longrightarrow LiF\ (s) + 2HF\ (sol) + POF_3\ (g) \qquad (2)$$

According to equation (1), $LiPF_6$ forms an equilibrium with LiF and PF_5. The strong Lewis acid PF_5 will accelerate the decomposition of Lewis base carbonate electrolytes. Besides, the hygroscopic nature of $LiPF_6$ facilitates the production of HF, as shown in equation (2), which can etch the Li metal surface. Moreover, a previous study showed that the SEI formed by LP40 is mosaic-like while the SEI formed by IPN-5PAN-G has an ideal hierarchical structure,[9, 55-58] which

further explains why the prepared IPN-5PAN-G can stabilize lithium metal anode and deliver high CE over cycling.

To demonstrate the concept of a room temperature high voltage battery, $LiNi_{0.6}Mn_{0.2}Co_{0.2}O_2$ battery was assembled using IPN-5PAN-G as both the separator and electrolytes. Before battery testing, CV of IPN-5PAN-G was measured, and 5 cycles were run between -0.5 V to 6 V (Figure S12). No oxidation was detected until 4.6 V, which is consistent with the report using diglyme/$LiNO_3$/LiBOB as the electrolyte.[33] The assembly of the full battery and operation voltage range were the same as previously described. Two current densities, 20 mA g^{-1} (0.1 C) and 100 mA g^{-1} (0.5 C) were selected, and the battery was run at 25 ºC. Figure 5a shows that the initial discharge capacity of 173 mAh g^{-1} and 146 mAh g^{-1} can be achieved at a current density of 20 mA g^{-1} and 100 mA g^{-1}, respectively. After 100 cycles, the discharge capacity of the cell running at 20 mA g^{-1} decays to 150 mAh g^{-1} (Figure 5b) and 110 mAh g^{-1} for the cell running at 100 mA g^{-1} (Figure 5c). The capacity retention rates are 86.7% and 75.3%, respectively. The average CE over 100 cycles is 97.6% and 97.1% for cells running at 20 mA g^{-1} and 100 mA g^{-1}. The evolution of the midpoint voltage of cells running at different current densities is shown in Figure 5b. The discharge midpoint voltage decays from 3.69 V to 3.64 V, and a retention rate of 98.6% for the cell running at 20 mA g^{-1} was achieved. When the current density increases to 100 mA g^{-1}, the midpoint voltage decreased from 3.64 V to 3.52 V, with a retention rate of 96.7%. Compared with IPN-5PAN SPEs, the battery using IPN-5PAN-G can enable the cycling at lower temperature, deliver a higher capacity at higher current rates, and prolong cycling. However, the initial midpoint voltage did not increase, 3.69 V for IPN-5PAN-G and 3.71 V for IPN-5PAN. As mentioned before, the voltage midpoint decay is attributed to the charge-transfer resistance at the interface. The IPN GPE outperforms liquid electrolytes in LMBs. Zheng *et al.* showed the

performance of LP 40 with $LiNi_{0.5}Mn_{0.3}Co_{0.2}O_2$ cathodes. At the current density of 180 mA g^{-1}, the cell could deliver an initial capacity of 154 mAh g^{-1} and a sharp capacity decay occurs after 40 cycles. After 100 cycles, the capacity retention rate was only 14%. When using fluoroethylene carbonate as the electrolyte additive, the cell showed a capacity retention rate of 65% after 100 cycles.[59] Choudhury *et al.* employed the same liquid electrolyte as the IPN-5PAN-G with HFiP as additive and coupled it with $LiNi_{0.6}Mn_{0.2}Co_{0.2}O_2$ cathode. At 0.2 C, the cell can be cycled for 200 cycles with over 80% capacity retained and CE of over 98%.[33] A lack of additives to protect cathode materials in cycling might be reason of relatively lower CE. Figure S13 shows the Nyquist plots measured by EIS for cells using IPN-5PAN-G at different cycles. The bulk resistance, charge-transfer resistance in electrolyte increases during cycling for the cell using IPN GPE which is likely owing to the depletion of the electrolyte. Figure S14 shows the electrolyte uptake rate with soaking time for the polymer matrix of IPN-5PAN-G and Celgard. Celgard can quickly reach the equilibrium state and the final uptake is 120 wt.%. On the other hand, the polymer matrix needs a much longer time and can only reach an uptake of 70 wt.%. Compared with Celgard, polymer matrix has a denser structure, and the mechanism of liquid uptake is via swelling of polymer chains. The lack of sufficient electrolytes in IPN GPEs likely induces the electrolyte depletion over cycling, which may account for the capacity and CE diverging after long cycling (> 100).

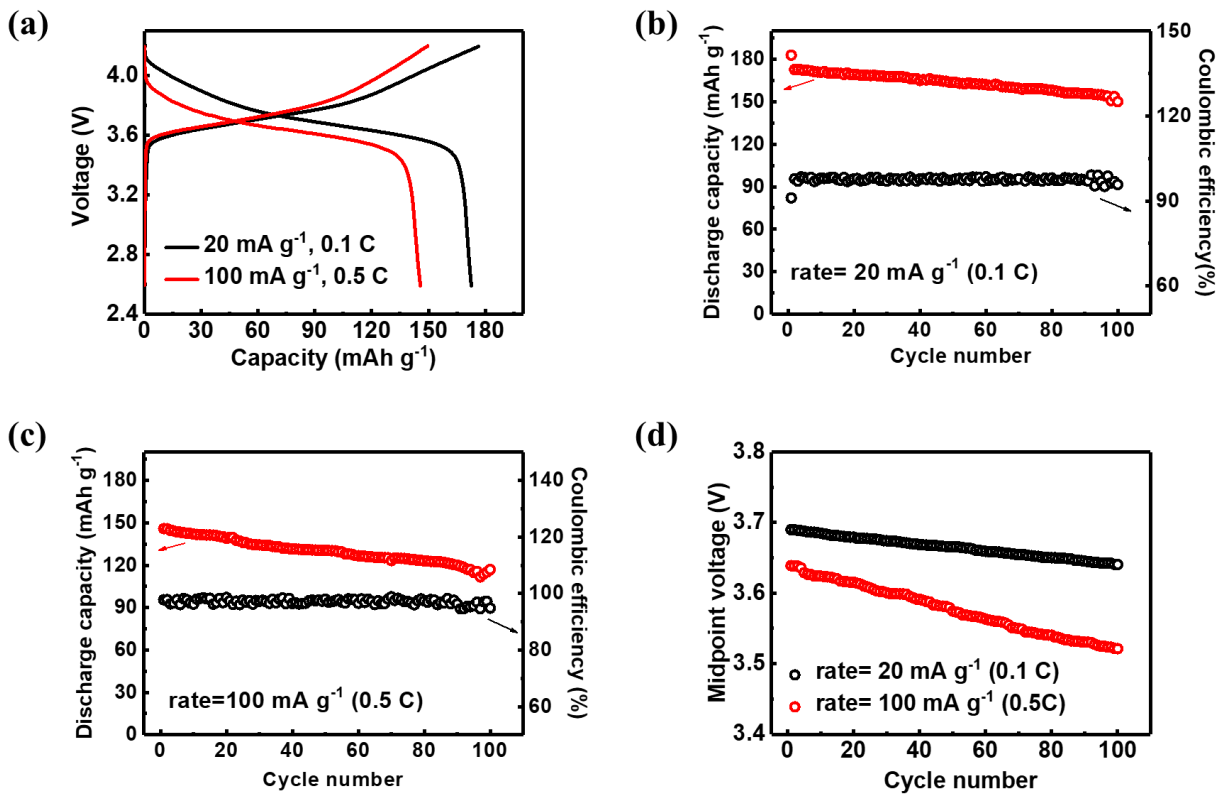

Figure 5. Performance of battery NMC-622|IPN-5PAN-G|Li at RT. (a) Initial cycle profiles at different current densities/ C rates. Cycling stability of discharge capacity and CE at (b) 20 mA g^{-1} and (c) 100 mA g^{-1}. (d) Evolution of midpoint voltage with cycle number at different current densities.

Conclusion

In summary, high voltage SPE was successfully synthesized by incorporating linear PAN into a PEO-based hybrid network to form IPN SPEs. The prepared IPN SPEs are robust, flexible, and electrochemically stable up to 5.1 V. Our results showed that the SPE cycling stability again lithium metal anode was significantly improved by PAN addition, and the effect of PAN on SEI was analyzed by XPS. $LiNi_{0.6}Mn_{0.2}Co_{0.2}O_2$ SSLMBs were successfully fabricated and could deliver a high capacity of over 150 mAh g^{-1}. To further improve the battery's performance, IPN-based GPEs were also prepared, and room temperature $LiNi_{0.6}Mn_{0.2}Co_{0.2}O_2$ batteries were

successfully fabricated. Initial discharge capacity over 170 mAh g^{-1} was obtained, and the IPN GPE showed significantly improved stability compared with the LP40 control. The significantly improved performance was attributed to the uniform IPN structure and the high resistance to oxidation of PAN. Therefore, our work demonstrated that IPN-based SPEs and GPEs, by combining selected primary and secondary networks, are promising for high voltage LMB applications.

Experimental

Materials. Octa-POSS, poly(acrylonitrile) (PAN) (M_n = 150k g mol^{-1}), poly (ethylene glycol) bis(3-aminopropyl) terminated (M_n = 2,000 g mol^{-1}), LiTFSI, LiBOB, $LiNO_3$, diglyme and dimethylformamide were purchased from Sigma-Aldrich. Carbon black and copper foil were obtained from MTI Corporation. Pristine lithium metal foil was purchased from Alfa Aesar.

Synthesis of IPN-PAN and IPN-PAN-G. For IPN-PAN, a series of PEG, POSS, PAN, and LiTFSI was dissolved in DMF. The molar ratio between PEG and POSS was fixed at 4. The weight percentage of PAN over the network (PEG+POSS+PAN) was tuned from 2% to 10%. The ratio between the EO group and LiTFSI was fixed at 10:1. The solution was stirred at 50 ºC for 2 hrs, cast on a glass slide, transferred into a vacuum oven, cured at 90 ºC for overnight, and then 120 ºC for another 2 hrs. The thickness of the film was approximately 70 μm.

For IPN-PAN-G, LiTFSI was not included when synthesizing the film. After thoroughly drying, the film was soaked in diglyme-$LiNO_3$-LiBOB for one day before use. All processes were conducted in an Ar-filled glove box. Both oxygen and moisture levels were below 0.5 ppm.

Differential scanning calorimetry. DSC experiments were performed using a TA Instrument Q2000 DSC with Refrigerated Cooling System RCS90 and N_2 purge gas and samples (2-3 mg) were sealed in Tzero pans. For IPN SPEs, the samples were first heated to 90 ºC, cooled to -90 ºC, and then heated to 90 ºC. Heating and cooling rates were 10 ºC min^{-1}. For the control PAN SPE, the scanning range was between -60 ºC and 150 ºC. The heating rate was 50 ºC min^{-1} and the cooling rate was 1 ºC min^{-1}. Data from second heating were used for analysis.

Ionic conductivity. Ionic conductivity was measured by EIS using Princeton Applied Research Parstat 2273 Potentiostat with a Powersuit software. The frequency range was from 1 MHz to 0.1 Hz. SPE films were cut into square shapes and sandwiched between two stainless steel electrodes. Temperature-varied EIS were measured from room temperature to 90 ºC. The bulk resistance of SPE was calculated by fitting an equivalent Randles circuit to the Nyquist plot. Ionic conductivity was determined using equation $\sigma = L/(A \times R)$ where L and A are sample thickness and contact area, respectively. Three batches of each sample were measured, and the average values were reported.

Electrochemical test. CV was measured using Li| stainless steel 2032-type coin cells. The scan rate was 0.5 mV s^{-1} and the scan range was between -0.5 V to 6 V. Li metal anode CE was measured

using Li| Cu 2032-type coin cells. The current density was 0.5 mA cm^{-2} and the plating capacity was 0.5 mAh cm^{-2}. $LiNi_{0.6}Mn_{0.2}Co_{0.2}O_2$ was synthesized using a coprecipitation and calcination method.[45] The batteries were cycled between 2.5-4.2 V. The battery using IPN SPE was cycled at 90 ºC and the battery using IPN GPE was cycled at 25 ºC. All galvanostatic cycling measurements were conducted using an Arbin battery tester.

SEM and XPS. SEM experiments were performed using a Zeiss Supra 50VP scanning electron microscope. XPS experiments were performed on Physical Electronics VersaProbe 5000 using high power 100 µm 100 W X-ray beam for acquisition. 2 kV Ar ion was used for sputtering or etching the surface if needed. The lithium electrode samples were sealed in Ar-filled chamber during all transfer process to avoid oxidation.

SAXS. SAXS experiments were conducted at the National Synchrotron Light Source II (NSLS-II), Brookhaven National Laboratory, utilizing the Complex Materials Scattering (CMS) beamline. The x-ray wavelength was set to 0.918 Å (13.5 keV).

ASSOCIATED CONTENT

Supporting Information

The following files are available free of charge. SAXS, CV, XPS, SEM XRD, and EIS results of selected samples. Supplementary Figures S1-S14 and Supplementary Table S1 and S2.

AUTHOR INFORMATION

Corresponding Author

*Christopher Y. Li – Department of Materials Science and Engineering, Drexel University, Philadelphia, PA 19104, USA; E-mail: chrisli@drexel.edu

Author Contributions

The manuscript was written through the contributions of all authors. All authors have given approval to the final version of the manuscript.

Notes

The authors declare no competing financial interest.

ACKNOWLEDGMENT

We are grateful for the support from the National Science Foundation through grants CBET 1603520 and CBET 2033882. We thank Mark Staub, Masafumi Fukuto and Ruipeng Li for their assitance in SAXS experiments. This research used the Complex Materials Scattering (CMS/11-BM) beamline, operated by the National Synchrotron Light Source II at Brookhaven National Laboratory, which is support-ed by the U.S. Department of Energy, Office of Science, Office of Basic Energy Sciences, under Contract DE-SC0012704.

REFERENCES

1. Julien, C. M.; Mauger, A.; Zaghib, K.; Groult, H., Comparative issues of cathode materials for li-ion batteries. *Inorganics* **2014,** *2*, 132-154.
2. Andre, D.; Kim, S.-J.; Lamp, P.; Lux, S. F.; Maglia, F.; Paschos, O.; Stiaszny, B., Future generations of cathode materials: An automotive industry perspective. *J. Mater. Chem. A* **2015,** *3*, 6709-6732.
3. Sano, H.; Kitta, M.; Matsumoto, H., Effect of charge transfer resistance on morphology of lithium electrodeposited in ionic liquid. *J. Electrochem. Soc.* **2016,** *163*, D3076-D3079.
4. Steiger, J.; Kramer, D.; Mönig, R., Mechanisms of dendritic growth investigated by in situ light microscopy during electrodeposition and dissolution of lithium. *J. Power Sources* **2014,** *261*, 112-119.
5. Tang, C.-Y.; Dillon, S., In situ scanning electron microscopy characterization of the mechanism for li dendrite growth. *J. Electrochem. Soc.* **2016,** *163*, A1660-A1665.
6. Cheng, X.-B.; Zhang, R.; Zhao, C.-Z.; Zhang, Q., Toward safe lithium metal anode in rechargeable batteries: A review. *Chem. Rev.* **2017,** *117*, 10403-10473.
7. Cheng, X. B.; Zhang, R.; Zhao, C. Z.; Wei, F.; Zhang, J. G.; Zhang, Q., A review of solid electrolyte interphases on lithium metal anode. *Adv. Sci.* **2016,** *3*, 1500213.
8. Lin, D.; Liu, Y.; Cui, Y., Reviving the lithium metal anode for high-energy batteries. *Nat. Nanotechnol.* **2017,** *12*, 194-206.
9. Xu, K., Nonaqueous liquid electrolytes for lithium-based rechargeable batteries. *Chem. Rev.* **2004,** *104*, 4303-4418.
10. Xu, K., Electrolytes and interphases in li-ion batteries and beyond. *Chem. Rev.* **2014,** *114*, 11503-11618.
11. Hallinan Jr, D. T.; Balsara, N. P., Polymer electrolytes. *Ann. Rev. Mater. Res.* **2013,** *43*, 503-525.
12. Tikekar, M. D.; Choudhury, S.; Tu, Z.; Archer, L. A., Design principles for electrolytes and interfaces for stable lithium-metal batteries. *Nat. Energy* **2016,** *1*, 16114.

13. Li, X.; Zheng, Y.; Pan, Q.; Li, C. Y., Polymerized ionic liquid-containing interpenetrating network solid polymer electrolytes for all-solid-state lithium metal batteries. *ACS Appl. Mater. Inter.* **2019**.
14. Pan, Q.; Barbash, D.; Smith, D. M.; Qi, H.; Gleeson, S. E.; Li, C. Y., Correlating electrode–electrolyte interface and battery performance in hybrid solid polymer electrolyte-based lithium metal batteries. *Adv. Energy Mater.* **2017,** *7*, 1701231.
15. Pan, Q.; Smith, D. M.; Qi, H.; Wang, S.; Li, C. Y., Hybrid electrolytes with controlled network structures for lithium metal batteries. *Adv. Mater.* **2015,** *27*, 5995-6001.
16. Pan, Q.; Zheng, Y.; Kota, S.; Huang, W.; Wang, S.; Qi, H.; Kim, S.; Tu, Y.; Barsoum, M. W., 2d mxene-containing polymer electrolytes for all-solid-state lithium metal batteries. *Nanoscale Adv.* **2019,** *1*, 395-402.
17. Zheng, Y.; Pan, Q.; Clites, M.; Byles, B. W.; Pomerantseva, E.; Li, C. Y., High-capacity all-solid-state sodium metal battery with hybrid polymer electrolytes. *Adv. Energy Mater.* **2018,** *8*, 1801885.
18. Li, X.; Cheng, S.; Zheng, Y.; Li, C. Y., Morphology control in semicrystalline solid polymer electrolytes for lithium batteries. *Mol. Sys. Des. Engin.* **2019,** *4*, 793-803.
19. Li, X.; Zheng, Y.; Li, C. Y., Dendrite-free, wide temperature range lithium metal batteries enabled by hybrid network ionic liquids. *Energy Storage Mater.* **2020,** *29*, 273-280.
20. Heine, J.; Hilbig, P.; Qi, X.; Niehoff, P.; Winter, M.; Bieker, P., Fluoroethylene carbonate as electrolyte additive in tetraethylene glycol dimethyl ether based electrolytes for application in lithium ion and lithium metal batteries. *J. Electrochem. Soc.* **2015,** *162*, A1094-A1101.
21. Guo, J.; Wen, Z.; Wu, M.; Jin, J.; Liu, Y., Vinylene carbonate–lino3: A hybrid additive in carbonic ester electrolytes for sei modification on li metal anode. *Electrochem. Commun.* **2015,** *51*, 59-63.
22. Patel, S. N., 100th anniversary of macromolecular science viewpoint: Solid polymer electrolytes in cathode electrodes for lithium batteries. Current challenges and future opportunities. *ACS Macro Lett. 10*, 141-153.
23. Hallac, B.; Luo, Y., Polysulfone coating for high voltage lithium-ion cells. Google Patents: 2017.
24. Cheng, Q.; Cui, Z.; Li, J.; Qin, S.; Yan, F.; Li, J., Preparation and performance of polymer electrolyte based on poly(vinylidene fluoride)/polysulfone blend membrane via thermally induced phase separation process for lithium ion battery. *J. Power Sources* **2014,** *266*, 401-413.
25. Choe, H. S.; Carroll, B. G.; Pasquariello, D. M.; Abraham, K. M., Characterization of some polyacrylonitrile-based electrolytes. *Chem. Mater.* **1997,** *9*, 369-379.
26. Kuo, P.-L.; Wu, C.-A.; Lu, C.-Y.; Tsao, C.-H.; Hsu, C.-H.; Hou, S.-S., High performance of transferring lithium ion for polyacrylonitrile-interpenetrating crosslinked polyoxyethylene network as gel polymer electrolyte. *ACS Appl. Mater. Inter.* **2014,** *6*, 3156-3162.
27. Yuan, F.; Chen, H.-Z.; Yang, H.-Y.; Li, H.-Y.; Wang, M., Pan–peo solid polymer electrolytes with high ionic conductivity. *Mater. Chem. Phys.* **2005,** *89*, 390-394.
28. Chen-Yang, Y. W.; Chen, H. C.; Lin, F. J.; Chen, C. C., Polyacrylonitrile electrolytes: 1. A novel high-conductivity composite polymer electrolyte based on pan, liclo4 and α-al2o3. *Solid State Ionics* **2002,** *150*, 327-335.
29. Yang, C. R.; Perng, J. T.; Wang, Y. Y.; Wan, C. C., Conductive behaviour of lithium ions in polyacrylonitrile. *J. Power Sources* **1996,** *62*, 89-93.

30. Li, X.; Zheng, Y.; Duan, Y.; Shang, M.; Niu, J.; Li, C. Y., Designing comb-chain crosslinker-based solid polymer electrolytes for additive-free all-solid-state lithium metal batteries. *Nano Lett.* **2020,** *20*, 6914-6921.
31. Aurbach, D.; Pollak, E.; Elazari, R.; Salitra, G.; Kelley, C. S.; Affinito, J., On the surface chemical aspects of very high energy density, rechargeable li–sulfur batteries. *J. Electrochem. Soc.* **2009,** *156*, A694.
32. Li, W.; Yao, H.; Yan, K.; Zheng, G.; Liang, Z.; Chiang, Y.-M.; Cui, Y., The synergetic effect of lithium polysulfide and lithium nitrate to prevent lithium dendrite growth. *Nat. Commun.* **2015,** *6*, 7436.
33. Choudhury, S.; Tu, Z.; Nijamudheen, A.; Zachman, M. J.; Stalin, S.; Deng, Y.; Zhao, Q.; Vu, D.; Kourkoutis, L. F.; Mendoza-Cortes, J. L.; Archer, L. A., Stabilizing polymer electrolytes in high-voltage lithium batteries. *Nat. Commun.* **2019,** *10*, 3091.
34. Zhao, Q.; Chen, P.; Li, S.; Liu, X.; Archer, L. A., Solid-state polymer electrolytes stabilized by task-specific salt additives. *J. Mater. Chem. A* **2019,** *7*, 7823-7830.
35. von Cresce, A.; Xu, K., Electrolyte additive in support of 5 v li ion chemistry. *J. Electrochem. Soc.* **2011,** *158*, A337.
36. Zheng, Y.; Li, X.; Li, C. Y., A novel de-coupling solid polymer electrolyte via semi-interpenetrating network for lithium metal battery. *Energy Storage Mater.* **2020,** *29*, 42-51.
37. Xu, H.; Zhang, H.; Ma, J.; Xu, G.; Dong, T.; Chen, J.; Cui, G., Overcoming the challenges of 5 v spinel lini0. 5mn1. 5o4 cathodes with solid polymer electrolytes. *ACS Energy Lett.* **2019,** *4*, 2871-2886.
38. Wang, C.; Wang, T.; Wang, L.; Hu, Z.; Cui, Z.; Li, J.; Dong, S.; Zhou, X.; Cui, G., Differentiated lithium salt design for multilayered peo electrolyte enables a high-voltage solid-state lithium metal battery. *Adv. Sci.* **2019,** *6*, 1901036.
39. Lv, Z.; Zhou, Q.; Zhang, S.; Dong, S.; Wang, Q.; Huang, L.; Chen, K.; Cui, G., Cyano-reinforced in-situ polymer electrolyte enabling long-life cycling for high-voltage lithium metal batteries. *Energy Storage Mater.* **2021,** *37*, 215-223.
40. Schaefer, D. W.; Justice, R. S., How nano are nanocomposites? *Macromolecules* **2007,** *40*, 8501-8517.
41. Chu, B.; Hsiao, B. S., Small-angle x-ray scattering of polymers. *Chem. Rev.* **2001,** *101*, 1727-1762.
42. Meyer, W. H., Polymer electrolytes for lithium-ion batteries. *Adv. Mater.* **1998,** *10*, 439-448.
43. Wu, Y.; Fang, Q.; Yi, X.; Liu, G.; Li, R.-W., Recovery of gold from hydrometallurgical leaching solution of electronic waste via spontaneous reduction by polyaniline. *Prog. Nat. Sci.* **2017,** *27*, 514-519.
44. Zhou, Y.; Su, M.; Yu, X.; Zhang, Y.; Wang, J.-G.; Ren, X.; Cao, R.; Xu, W.; Baer, D. R.; Du, Y.; Borodin, O.; Wang, Y.; Wang, X.-L.; Xu, K.; Xu, Z.; Wang, C.; Zhu, Z., Real-time mass spectrometric characterization of the solid–electrolyte interphase of a lithium-ion battery. *Nat. Nanotechnol.* **2020,** *15*, 224-230.
45. Ren, D.; Shen, Y.; Yang, Y.; Shen, L.; Levin, B. D. A.; Yu, Y.; Muller, D. A.; Abruña, H. D., Systematic optimization of battery materials: Key parameter optimization for the scalable synthesis of uniform, high-energy, and high stability lini0.6mn0.2co0.2o2 cathode material for lithium-ion batteries. *ACS Appl. Mater. Inter.* **2017,** *9*, 35811-35819.

46. Kaboli, S.; Demers, H.; Paolella, A.; Darwiche, A.; Dontigny, M.; Clément, D.; Guerfi, A.; Trudeau, M. L.; Goodenough, J. B.; Zaghib, K., Behavior of solid electrolyte in li-polymer battery with nmc cathode via in-situ scanning electron microscopy. *Nano Lett.* **2020,** *20*, 1607-1613.
47. Alexander, George V.; Rosero-Navarro, N. C.; Miura, A.; Tadanaga, K.; Murugan, R., Electrochemical performance of a garnet solid electrolyte based lithium metal battery with interface modification. *J. Mater. Chem. A* **2018,** *6*, 21018-21028.
48. Zhao, W.; Zheng, J.; Zou, L.; Jia, H.; Liu, B.; Wang, H.; Engelhard, M. H.; Wang, C.; Xu, W.; Yang, Y.; Zhang, J.-G., High voltage operation of ni-rich nmc cathodes enabled by stable electrode/electrolyte interphases. *Adv. Energy Mater.* **2018,** *8*, 1800297.
49. Noh, H.-J.; Youn, S.; Yoon, C. S.; Sun, Y.-K., Comparison of the structural and electrochemical properties of layered li[nixcoymnz]o2 (x = 1/3, 0.5, 0.6, 0.7, 0.8 and 0.85) cathode material for lithium-ion batteries. *J. Power Sources* **2013,** *233*, 121-130.
50. Leng, Y.; Ge, S.; Marple, D.; Yang, X.-G.; Bauer, C.; Lamp, P.; Wang, C.-Y., Electrochemical cycle-life characterization of high energy lithium-ion cells with thick li(ni0.6mn0.2co0.2)o2and graphite electrodes. *J. Electrochem. Soc.* **2017,** *164*, A1037-A1049.
51. Xia, Y.; Zheng, J.; Wang, C.; Gu, M., Designing principle for ni-rich cathode materials with high energy density for practical applications. *Nano Energy* **2018,** *49*, 434-452.
52. Kang, Y.; Deng, C.; Chen, Y.; Liu, X.; Liang, Z.; Li, T.; Hu, Q.; Zhao, Y., Binder-free electrodes and their application for li-ion batteries. *Nanoscale Research Letters* **2020,** *15*, 112.
53. Xu, C.; Märker, K.; Lee, J.; Mahadevegowda, A.; Reeves, P. J.; Day, S. J.; Groh, M. F.; Emge, S. P.; Ducati, C.; Layla Mehdi, B.; Tang, C. C.; Grey, C. P., Bulk fatigue induced by surface reconstruction in layered ni-rich cathodes for li-ion batteries. *Nat. Mater.* **2021,** *20*, 84-92.
54. Zhu, B.; Jin, Y.; Hu, X.; Zheng, Q.; Zhang, S.; Wang, Q.; Zhu, J., Poly(dimethylsiloxane) thin film as a stable interfacial layer for high-performance lithium-metal battery anodes. *Adv. Mater.* **2017,** *29*, 1603755.
55. Aurbach, D.; Ein‐Eli, Y.; Markovsky, B.; Zaban, A.; Luski, S.; Carmeli, Y.; Yamin, H., The study of electrolyte solutions based on ethylene and diethyl carbonates for rechargeable li batteries: Ii . Graphite electrodes. *J. Electrochem. Soc.* **1995,** *142*, 2882-2890.
56. Andersson, A. M.; Edström, K., Chemical composition and morphology of the elevated temperature sei on graphite. *J. Electrochem. Soc.* **2001,** *148*, A1100.
57. Edström, K.; Andersson, A. M.; Bishop, A.; Fransson, L.; Lindgren, J.; Hussénius, A., Carbon electrode morphology and thermal stability of the passivation layer. *J. Power Sources* **2001,** *97-98*, 87-91.
58. Peled, E.; Golodnitsky, D.; Ardel, G., Advanced model for solid electrolyte interphase electrodes in liquid and polymer electrolytes. *J. Electrochem. Soc.* **1997,** *144*, L208-L210.
59. Zhang, X.-Q.; Cheng, X.-B.; Chen, X.; Yan, C.; Zhang, Q., Fluoroethylene carbonate additives to render uniform li deposits in lithium metal batteries. *Adv. Funct. Mater.* **2017,** *27*, 1605989.

For Table of Contents Only

IPN SPE and IPN GPE